Crystal structure and ionic conductivity of Mg-doped apatite-type lanthanum silicates $La_{10}Si_{6-x}Mg_xO_{27-x}$ ($x = 0$–0.4)*

Yin Guang-Chao(尹广超), Yin Hong(殷 红), Zhong Lin-Hong(仲林红), Sun Mei-Ling(孙美玲), Zhang Jun-Kai(张俊凯), Xie Xiao-Jun(谢晓君), Cong Ri-Dong(丛日东), Wang Xin(王 欣), Gao Wei(高 伟)†, and Cui Qi-Liang(崔啟良)

State Key Laboratory of Superhard Materials, Jilin University, Changchun 130012, *China*

(Received 8 August 2013; revised manuscript received 22 October 2013; published online 20 February 2014)

Lanthanum silicates $La_{10}Si_{6-x}Mg_xO_{27-x}$ ($x = 0$–0.4) were prepared by solid state synthesis to investigate the effect of Mg doping on crystal structure and ionic conductivity. Rietveld analysis of the powder XRD patterns reveals that Mg substitution on Si site results in significant enlargement of channel triangles, favoring oxide-ion conduction. Furthermore, an increase of Mg concentration significantly influences the linear density of interstitial oxygen, which plays an important role in ionic conductivity. The Arrhenius plots of $La_{10}Si_{6-x}Mg_xO_{27-x}$ ($x = 0$–0.4) suggest that Mg-doped samples present higher conductivity and lower activation energy than non-doped $La_{10}Si_6O_{27}$, and $La_{10}Si_{5.8}Mg_{0.2}O_{26.8}$ exhibits the highest conductivity with a value of 3.0×10^{-2} S ·cm^{-1} at 700 °C. Such conductive behavior agrees well with the refined results. The corresponding mechanism has been discussed in this paper.

Keywords: solid oxide fuel cells, electrolyte, ionic conduction

PACS: 82.47.Ed, 82.45.Gj, 66.30.Dn **DOI:** 10.1088/1674-1056/23/4/048202

1. Introduction

The usage of apatite-type lanthanum silicates (ATLS) as novel electrolyte materials for intermediate temperature solid oxide fuel cells (IT-SOFCs) has achieved considerable worldwide interest due to clean energy conversion, high energy efficiency, and the potential for developing fuel cell devices,[1–16] ever since Nakayama *et al.* advocated it for the first time.[17] In contrast to the vacancy mechanism common to the fluorite- and perovskite-type oxide-ion conductors, such as doped ZrO_2 (e.g. YSZ) and doped $LaGaO_3$ (e.g. LSGM), which have been targeted for IT-SOFCs up to the present, a unique interstitial conduction mechanism is found in ATLS, making it even more attractive. Previous experimental and theoretical evidence identified that the structure of ATLS comprises isolated SiO_4 tetrahedra units with La ions located in 7- and 9-coordinate channel sites and the remaining oxide ions occupying one-dimensional channels running parallel to the hexagonal axis (space group $P6_3/m$). Moreover, such interstitial oxygenic sites at the periphery of the hexagonal channel close to the silicon groups are considered vital for the high oxide-ion conduction[18–20] needed in IT-SOFCs. It has been found that the conductivity of lanthanum silicates is very sensitive to the doping regime and the cation/anion nonstoichiometry.[21–29] Particularly, Mg as an ambi-site dopant can be substituted onto either La or Si sites depending on the starting composition. However, rather poor conductivity has been observed when Mg is doped on La sites, for example, the oxygen stoichiometric $La_9Mg_{0.5}Si_6O_{26}$, due to a lack of interstitial oxygenic site occupancy.[30] Thus, considering the limitations of Mg substitution on La site, doping on the Si site seems to be the most promising route for improving conductivity.

The previous investigations about Mg substituting on Si site, i.e., $La_{9.5}Si_{5.75}Mg_{0.25}O_{26}$ and $La_{9.67}Si_{5.5}Mg_{0.5}O_{26}$ led to a remarkable enhancement in conductivity, while maintaining the oxygen stoichiometry.[30] The local enlargement of oxide-ion channels induced by the corresponding increase in the size of the tetrahedral sites due to the larger size of Mg^{2+} compared to Si^{4+} has been linked to such elevated conductivity.[31–35] However, the presence of interstitial oxygen has been confirmed only qualitatively, by Rietveld analysis, unfortunately. Besides noticing the importance of Si sites in the conduction process, a detailed understanding of conduction mechanism has not been thoroughly established, because of a lack of quantitative data. Further study carried out by Ali *et al.* also proposed a diffusion path of oxide ions in excess-oxygen $La_{9.71}Si_{5.81}Mg_{0.18}O_{26.37}$, and reported a similar large enhancement in conductivity, but the effect of extra interstitial oxygen arising from increasing the La content while keeping the system electroneutral has been ignored.[36] Therefore, a systematic investigation of Mg substitution on the Si site while keeping La-cation stoichiometry, more particularly under the circumstance of excess oxygen, has not yet been accomplished. The correlation of crystal structural changes and interstitial oxygenic sites with increasing Mg dopant as well as the resulting conductivity behaviors must be clarified. In this context, the purpose of the present paper is to investigate the

*Project supported by the Scientific Research Foundation for the Returned Overseas Chinese Scholars, State Education Ministry.

†Corresponding author. E-mail: gwei@jlu.edu.cn

© 2014 Chinese Physical Society and IOP Publishing Ltd

crystal structure and the conductivity behavior of lanthanum silicates $La_{10}Si_{6-x}Mg_xO_{27-x}$ ($x = 0$–0.4). The interstitial oxygen density has been determined for the first time, which can contribute, as a supplement, to a fuller understanding of the conduction process: a quantitative understanding. As a wide range of dopants can be chosen for doping ATLS to improve its conductivity, a precise awareness of such interstitial oxygen density might enable new insight into conductivity behaviors, not only for the Mg-doped system of the present work, but also for many other possible doped systems of interest.

2. Experiments

Starting reactant powders of lanthanum oxide (La_2O_3, 99.99%), silicon oxide (SiO_2, 99.99%), and magnesium oxide (MgO, 99.99%) were weighed in the nominal composition of $La_{10}Si_{6-x}Mg_xO_{27-x}$ ($x = 0$–0.4). La_2O_3 powders were dried at 1000 °C for 2 h in advance. After weighing, the mixtures of reactants (La_2O_3, SiO_2, MgO) were ball milled in ethanol medium at the speed of 400 rpm for 8 h. After this process, the mixtures were dried, ground, and sifted to avoid agglomerated powders. The sifted powders were pressed under 100 MPa to form pellets, and then sintered at 1350 °C for 10 h. The sintered pellets were reground and reformed as pellets, and finally calcined at 1750 °C for 6 h again.

Phase characterizations of the samples were identified by X-ray diffractometer (XRD, Shimadu XRD-6000). The measurements were done using Cu-Kα radiation in the 2θ range of 20°–80° with a step size of 0.02° and counting time of 2 s. Rietveld analysis was performed on the powder XRD patterns using the GSAS program to perform the structural refinement. The bulk densities of samples were determined by the Archimedean method. Furthermore, the conductivities of samples were measured using a model Solartron 1260 impedance analyzer. Silver electrodes were coated on both surfaces of the sintered pellets and heated at 550 °C for 30 min. Impedance measurements were performed during heating from 450 °C to 700 °C in a frequency range from 0.1 Hz to 1 MHz with an increment of 50 °C, followed by an analysis of these results using Z-View software.

3. Results and discussion

The XRD patterns of the $La_{10}Si_{6-x}Mg_xO_{27-x}$ ($x = 0$–0.4) samples are shown in Fig. 1. It is obvious that all samples are identified as a single apatite phase, which is indexed with the hexagonal structure according to the JCPDS 53-0291. The strong and sharp diffraction peaks suggest that the as-prepared samples are well crystallized, and the diffraction peaks from impurities have not been detected, suggesting the high purity of the as-obtained products. The diffraction patterns of $La_{10}Si_{6-x}Mg_xO_{27-x}$ ($x = 0$–0.4) were refined by Rietveld analysis using the structural model with the symmetry of $P6_3/m$ (No. 176), and the fittings are shown in Fig. 2. Furthermore, the refined parameters of $La_{10}Si_{6-x}Mg_xO_{27-x}$ ($x = 0$–0.4) are shown in Table 1, and the refined crystal structure of $La_{10}Si_6O_{27}$ is shown in Fig. 3.

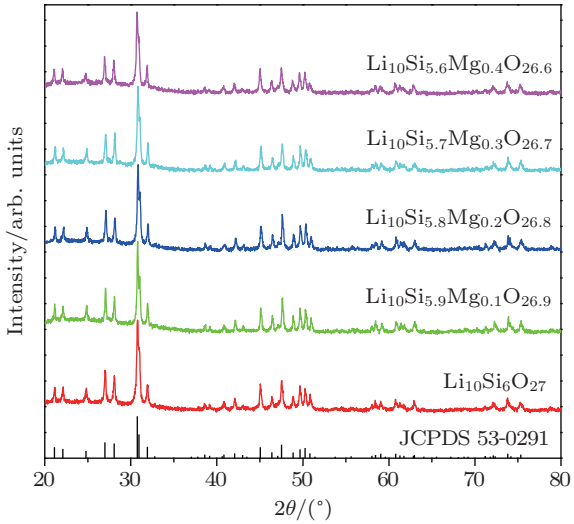


Fig. 1. (color online) The X-ray diffraction patterns of $La_{10}Si_{6-x}Mg_xO_{27-x}$ ($x = 0$–0.4) sintered at 1750 °C for 6 h.

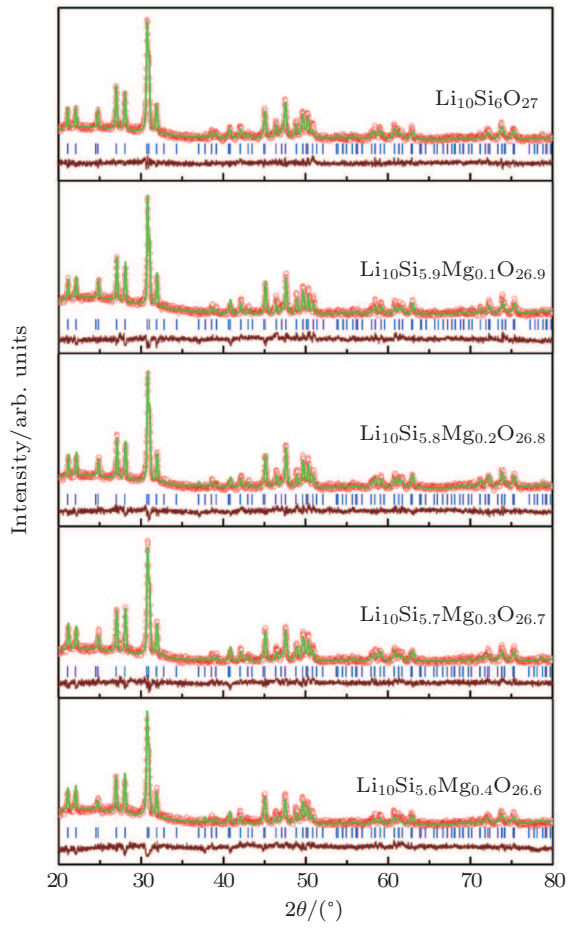


Fig. 2. (color online) Rietveld fitting patterns of $La_{10}Si_{6-x}Mg_xO_{27-x}$ ($x = 0$–0.4). Dots and lines: observed and calculated profile intensities, respectively.

Table 1. Refined structural parameters of $La_{10}Si_{6-x}Mg_xO_{27-x}$ ($x = 0$–0.4).

	$x = 0$	$x = 0.1$	$x = 0.2$	$x = 0.3$	$x = 0.4$
a, b/Å	9.7041(7)	9.7085(3)	9.7084(2)	9.7100(4)	9.7099(1)
c/Å	7.1625(5)	7.1703(4)	7.1755(4)	7.1775(4)	7.1787(1)
v/Å^3	584.14(2)	585.29(5)	585.70(7)	586.07(3)	586.15(0)
R_{wp}/%	6.2	5.3	4.1	3.2	4.0
R_p/%	3.9	3.5	2.9	1.8	2.3
La1 6h					
x	0.2324(9)	0.2310(7)	0.2313(7)	0.2317(8)	0.229(1)
y	–0.005(1)	–0.006(1)	–0.010(1)	–0.015(1)	–0.020(1)
z	0.2500	0.2500	0.2500	0.2500	0.2500
La2 4f					
x	0.3333	0.3333	0.3333	0.3333	0.3333
y	0.6667	0.6667	0.6667	0.6667	0.6667
z	–0.020(1)	–0.022 (1)	–0.022 (1)	–0.023(1)	–0.020(1)
Si/Mg 6h					
x	0.434 (2)	0.434(4)	0.426(2)	0.438(3)	0.442(3)
y	0.401(3)	0.402(4)	0.398(2)	0.404(2)	0.398(3)
z	0.2500	0.2500	0.2500	0.2500	0.2500
O1 6h					
x	0.339(5)	0.316(6)	0.327(6)	0.317(5)	0.330(9)
y	0.438(5)	0.445(8)	0.454(6)	0.445(6)	0.474(6)
z	0.2500	0.2500	0.2500	0.2500	0.2500
O2 6h					
x	0.633(8)	0.626(8)	0.616(7)	0.617(6)	0.611(9)
y	0.466(5)	0.449(6)	0.476(6)	0.444(5)	0.463(7)
z	0.2500	0.2500	0.2500	0.2500	0.2500
O3 12i					
x	0.355(3)	0.350(3)	0.353(4)	0.354(3)	0.356(4)
y	0.276(3)	0.272(3)	0.267(4)	0.279(3)	0.283(4)
z	0.089(3)	0.080(3)	0.091(3)	0.091(4)	0.091(4)
O4 2a					
(xyz)	(0 0 1/4)	(0 0 1/4)	(0 0 1/4)	(0 0 1/4)	(0 0 1/4)
O5 12i					
(xyz)	(0.1 0.23 0.62)	(0.1 0.23 0.62)	(0.1 0.23 0.62)	(0.1 0.23 0.62)	(0.1 0.23 0.62)

The cation structure of $La_{10}Si_6O_{27}$ consists of alternately layered triangles formed by the La1 6h and Si 6h, as can be clearly seen in Fig. 3. The La2 4f site is located between the La and Si triangles, as shown in Fig. 3. Three oxide ions (O1 6h, O2 6h, and O3 12i) are located close to the Si site and form an SiO_4 tetrahedron, the channel oxide ion (O4 2a) is located at the corner of the unit cell, and the interstitial oxide ion (O5 12i) is located in the middle of O4 2a and O3 12i. It is noticeable that both La1 6h and O3 12i, located along the c axis, form two triangles of different sizes, which constitute the main conduction channel triangles piled up along the c axis, as shown in Fig. 4. If the channel oxide ions (O4 2a) migrate inside hexagonal channels, they have to pass through the channel triangles; thus the conductivity is closely related to the sizes of triangles. Meanwhile, an interstitial conduction pathway of O3–O5–O4 is formed, perpendicular to the c axis, owing to their short interatomic distance (Fig. 4).[31] We believe that the interstitial oxygen density in the interstitial conduction pathway of O3–O5–O4 will also be found to play an important role in conduction.

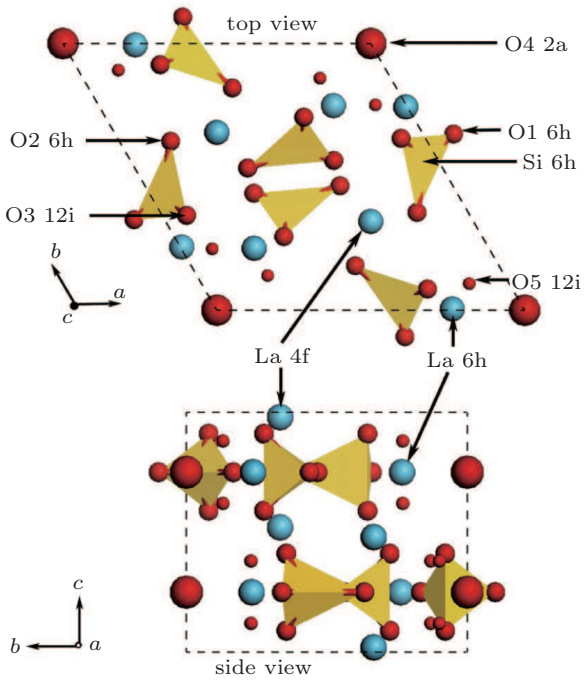


Fig. 3. (color online) The refined crystal structure of $La_{10}Si_6O_{27}$.

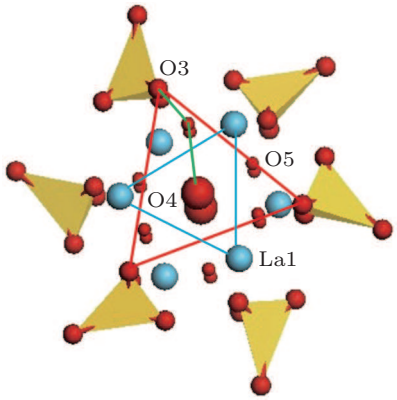


Fig. 4. (color online) The conduction channel triangles and interstitial conduction pathway of O4–O5–O3.

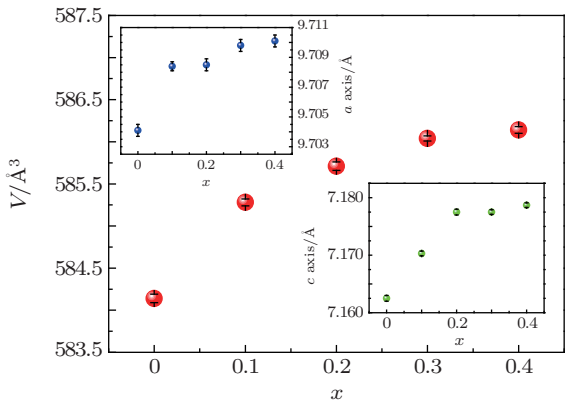


Fig. 5. (color online) The lattice parameters of $La_{10}Si_{6-x}Mg_xO_{27-x}$ ($x = 0$–0.4). Top-left inset is lattice parameter a, and bottom-right inset is lattice parameter c.

In the present study, Mg is substituted on Si site, owing to the low Mg doping level (Mg/Si< 0.11) and the high La/Si ratio (La/Si> 1.55).[30,31] Since the effective ionic radius of Mg^{2+} for fourfold coordination (0.57 Å) is much larger than that of Si^{4+} (0.26 Å), the Mg substitution could result in a significant lattice expansion, as shown in Fig. 5, which agrees well with previous investigations.[30,31] Furthermore, the interatomic distance and areas of channel triangles and the linear density of interstitial oxygen are shown in Table 2. The distances of both La1–La1 and O3–O3 increase remarkably, consistent with the lattice expansion. Due to the increase of La1–La1 and O3–O3 distances, both the La1 triangle and the O3 triangle are significantly enlarged, which can be defined by the area of the channel triangles (La1–La1–La1 and O3–O3–O3). As a result, the oxide-ion channels are significantly enlarged. However, as x increases, the length of the interstitial conduction pathway of O3–O5–O4 decreases first and then increases. In between, the distance reaches a minimum when $x = 0.2$. Such a pattern will dramatically affect the interstitial oxygen density in interstitial conduction pathways. The corresponding linear density of interstitial oxygen is calculated on the assumption that the number in an O4–O5–O3 conduction pathway for $La_{10}Si_6O_{27}$ is 1, and other samples are converted according to their corresponding oxygen content. In contrast to the length of the interstitial conduction pathway of O3–O5–O4, the linear density of interstitial oxygen first increases with increasing x, and when the value of x is more than 0.2 the linear density decreases with increasing x. Clearly, $La_{10}Si_{5.8}Mg_{0.2}O_{26.8}$ exhibits the highest linear density. The above changes will have a significant effect on conductivity.

Table 2. The interatomic distance (Å) and areas S (Å^2) of channel triangles, interstitial oxygen number N, and linear density LD (Å^{-1}) of interstitial oxide ions.

	$x = 0$	$x = 0.1$	$x = 0.2$	$x = 0.3$	$x = 0.4$
La1–La1	3.760	3.943	3.985	4.036	4.049
O3–O3	5.276	5.359	5.370	5.438	5.483
O3–O5–O4	3.501	3.474	3.440	3.512	3.540
S_{La1}	6.121	6.732	6.876	7.053	7.099
S_{O3}	12.05	12.44	12.49	12.81	13.02
N	1.000	0.996	0.992	0.989	0.985
LD	0.286	0.287	0.289	0.282	0.278

In order to more distinctly clarify the correlation of crystal structural changes and ionic conductivity, the conductivities of $La_{10}Si_{6-x}Mg_xO_{27-x}$ ($x = 0$–0.4) are investigated by AC electrical impedance spectroscopy. The obtained complex impedance plots of $La_{10}Si_{5.8}Mg_{0.2}O_{26.8}$ pellets, measured at 500 °C and 600 °C, are shown in Fig. 6. At 500 °C, the plots exhibit a partial arc and a clear arc. With the temperature increasing to 600 °C, the plots exhibit only a clear arc. In order to distinguish the contributions of bulk, grain boundary, and electrode, the corresponding contributions have been managed using the Z-View software to model the impedance spectrum of an equivalent circuit including four serial R_i and $(CPE)_i$ parallels (i is b for bulk, gb for grain boundary, total for bulk and grain boundary, and elec for electrode). At 500 °C, the fitting leads to $CPE_{gb} \approx 2.8\times10^{-7}$ F·cm^{-1} and $CPE_{elec} \approx 3.1\times10^{-5}$ F·cm^{-1}; thus they are ascribed to the contributions of grain boundary and electrode, respectively. Up to 600 °C, the fitting leads to $CPE_{elec} \approx 6.8\times10^{-5}$ F·cm^{-1}, so it is ascribed to the contribution of electrode. Disappearance of the arc corresponds to the grain boundary contribution in this situation, indicating that oxide ions can diffuse through the entire thickness of the bulk and the grain boundary. The impedance spectroscopy plots of other samples show trends very similar to that illustrated in Fig. 6.

The corresponding conductivity is converted by the resistance R_{total} ($R_b + R_{gb}$) using Eq. (1), and the activation energy is calculated by the Arrhenius equation (2):

$$\sigma = l/(R_{total} * S), \tag{1}$$

$$\sigma = \sigma_0 * \exp[-E_a/(k * T)]/T, \tag{2}$$

where l, S, σ, σ_0, E_a, and T are, respectively, the sample thickness, the electrode area of the sample surface, the conductivity, pre-exponential factor, activation energy, Boltzmann constant, and absolute temperature.

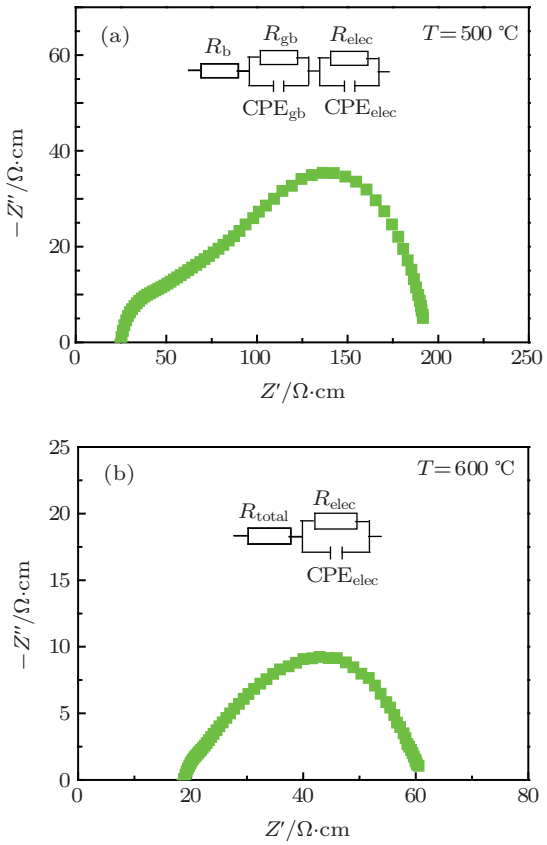


Fig. 6. (color online) The complex impedance plots measured at 500 °C (a), 600 °C (b) for the $La_{10}Si_{5.8}Mg_{0.2}O_{26.8}$ pellets sintered at 1750 °C for 6 h, and the corresponding schematic equivalent circuits.

The total conductivity (500 °C and 700 °C), the activation energy and the relative density of pellets are summarized in Table 3, and the Arrhenius plots of $La_{10}Si_{6-x}Mg_xO_{27-x}$ ($x = 0$–0.4) are shown in Fig. 7. It is clear that all the Mg-substituted samples display a higher conductivity than $La_{10}Si_6O_{27}$. Among the Mg-substituted samples, the conductivity is first enhanced with increasing x ($x \leq 0.2$), and when the value of x is greater than 0.2, the conductivity displays a slight reduction with increasing x ($0.2 \leq x \leq 0.4$). $La_{10}Si_{5.8}Mg_{0.2}O_{26.8}$ exhibits the highest conductivity with a value of 3.0×10^{-2} S· cm^{-1} at 700 °C. This conductive result should be attributed to the structural changes, and agrees well with our refined results above. The Mg substitution clearly enlarges the oxide-ion channels, as confirmed by the enhancement of the channel triangles' area (Table 2), which can reduce the channel oxide ion migration energies. As a result, the activation energy will decrease significantly, and the conductivity will be enhanced significantly.[30–33,35,36] Therefore, the Mg-substituted samples display a higher conductivity and a lower activation energy (Table 3) than non-doped compound $La_{10}Si_6O_{27}$. Based on the enlargement of oxide-ion channels, the linear density of interstitial oxygen in O3–O5–O4 conduction pathways takes an important role in conductivity, because it can affect the migration of oxide ions (O4 and O3), which can account for the conductive behavior of Mg-substituted samples. The conductive behavior of Mg-substituted samples is in a good agreement with the changes of the linear density of interstitial oxygen, and $La_{10}Si_{5.8}Mg_{0.2}O_{26.8}$ exhibits the highest conductivity, owing to its highest linear density. A similar strong dependence of the conductivity on carrier density was observed in many comparable studies.[37–40] The above results will be helpful for understanding the effect of Mg substitution on crystal structure and ionic conductivity.

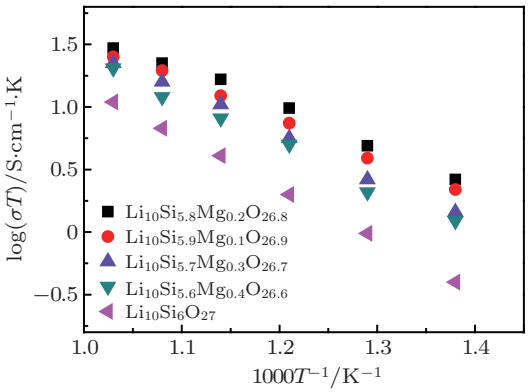


Fig. 7. (color online) The Arrhenius plots for total conductivities of $La_{10}Si_{6-x}Mg_xO_{27-x}$ ($x = 0$–0.4) sintered at 1750 °C for 6 h.

Table 3. The values of the relative density of pellets, the conductivity (500 °C and 700 °C) and the activation energy of $La_{10}Si_{6-x}Mg_xO_{27-x}$ ($x = 0$–0.4).

Composition	D_R/%	σ(500 °C)/S·cm^{-1}	σ(700 °C)/S·cm^{-1}	E_a/eV
$La_{10}Si_{5.9}Mg_{0.1}O_{26.9}$	91.4	5.0×10^{-3}	2.6×10^{-2}	0.62
$La_{10}Si_{5.8}Mg_{0.2}O_{26.8}$	91.3	6.4×10^{-3}	3.0×10^{-2}	0.61
$La_{10}Si_{5.7}Mg_{0.3}O_{26.7}$	92.2	3.4×10^{-3}	2.3×10^{-2}	0.70
$La_{10}Si_{5.6}Mg_{0.4}O_{26.6}$	90.9	2.7×10^{-3}	2.1×10^{-2}	0.69
$La_{10}Si_6O_{27}$	90.2	1.4×10^{-3}	1.2×10^{-2}	0.80

4. Conclusions

We investigated the relations between the conductivity and the structural changes caused by Mg substitution on Si site via $La_{10}Si_{6-x}Mg_xO_{27-x}$ ($x = 0$–0.4) samples. Besides an obvious lattice expansion being observed as Mg is substituted for Si, both the La1 and O3 channel triangles are significantly enlarged. As a result, the oxide-ion channels en-

large which leads to lower migration energies of channel oxide ions. Therefore, all Mg-substituted samples display higher conductivity and lower activation energy than $La_{10}Si_6O_{27}$. Furthermore, the conductivity of Mg-substituted samples first increases with increasing x, yet when the value of x is more than 0.2, the conductivity decreases with increasing x; and $La_{10}Si_{5.8}Mg_{0.2}O_{26.8}$ exhibits the highest conductivity with a value of 3.0×10^{-2} S·cm^{-1} at 700 °C. Such a pattern of conductivity behavior is in good agreement with the changes of the linear density of interstitial oxygen.

References

[1] Santos M, Alves C, Oliveira F A C, Marcelo T, Mascarenhas J, Cavaleiro A and Trindade B 2013 *Journal of Power Sources* **231** 146

[2] Liu W, Yamaguchi S, Tsuchiya T, Miyoshi S, Kobayashi K and Pan W 2013 *Journal of Power Sources* **235** 62

[3] Fukuda K, Asaka T, Okino M, Berghout A, Béchade E, Masson O, Julien I and Thomas P 2012 *Solid State Ionics* **217** 40

[4] Matsui T, Mineshige A, Funahashi T, Mieda H, Daiko Y, Kobune M, Yoshioka H and Yazawa T 2012 *Journal of Power Sources* **217** 170

[5] Gao W, Li W Y, Liao H L and Coddet C 2011 *Journal of Thermal Pray Technology* **20** 888

[6] Gasparyan H, Neophytides S, Niakolas D, Stathopoulos V, Kharlamova T, Sadykov V, Van der Biest O, Jothinathan E, Louradour E, Joulin J P and Bebelis S 2011 *Solid State Ionics* **192** 158

[7] Malavasi L, Fisher C A J and Islam M S 2010 *Chem. Soc. Rev.* **39** 4370

[8] Marrero-López D, Martín-Sedeño M C, Ruiz-Morales J C, Núñez P, Aranda M A G and Ramos-Barrado J R 2010 *Journal of Power Sources* **195** 2496

[9] Yang S D, Shen C M, Tong H, He W, Zhang X G and Gao H J 2011 *Chin. Phys. B* **20** 113301

[10] Ding H, Shi X Z, Shen C M, Hui C, Xu Z C, Li C, Tian Y, Wang D K and Gao H J 2010 *Chin. Phys. B* **19** 106104

[11] Kendrick E, Headspith D, Orera A, Apperley D C, Smith R I, Francesconi M G and Slater P R 2009 *J. Mater. Chem.* **19** 749

[12] Mineshige A, Nakao T, Kobune M, Yazawa T and Yoshioka H 2008 *Solid State Ionics* **179** 1009

[13] Gao W, Liao H L and Coddet C 2008 *Journal of Power Sources* **179** 739

[14] Tolchard J R, Slater P R and Islam M S 2007 *Adv. Funct. Mater.* **17** 2564

[15] Yoshioka H 2006 *J. Alloys Compd.* **408** 649

[16] Okudera H, Masubuch Y, Kikkawa S and Yoshiasa A 2005 *Solid State Ionics* **176** 1473

[17] Nakayama S, Kageyama T, Aono H and Sadaoka Y 1995 *J. Mater. Chem.* **5** 1801

[18] Li B, Liu W and Pan W 2010 *J. Power Sources* **195** 2196

[19] Béchade E, Masson O, Iwata T, Julien I, Fukuda K, Thomas P and Champion E 2009 *Chem. Mater.* **21** 2508

[20] Kendrick E, Islam M S and Slater P R 2007 *J. Mater. Chem.* **17** 3104

[21] Fukuda K, Asaka T, Ishizawa N, Mino H, Urushihara D, Berghout A, Bechade E, Masson O, Julien I and Thomas P 2012 *Chem. Mater.* **24** 2611

[22] Shi Q L, Lu L H, Jin H J, Zhang H and Zeng Y W 2012 *Mater. Res. Bull.* **47** 719

[23] Nallamuthu N, Prakash I, Satyanarayana N and Venkateswarlu M 2011 *J. Alloys Compd.* **509** 1138

[24] Gasparyan H, Neophytides S, Niakolas D, Stathopoilos V, Kharlamova T, Sadykov V, Van der Biest O, Jothinathan E, Louradour E, Joulin J P and Bebelis S 2011 *Solid State Ionics* **192** 158

[25] Jothinathan E, Vanmeensel K, Vleuggels J and Van der Biest O 2010 *J. Alloys Compd.* **495** 552

[26] Dru S, Meillot E, Wittmann-Teneze K, Benoit R and Saboungi M L 2010 *Surface & Coatings Technology* **205** 1060

[27] Jiang S P, Zhang L, He H Q, Yap R K and Xiang Y 2009 *J. Power Sources* **189** 972

[28] Kharlamova T, Pavlova S, Sadykov V, Krieger T, Batuev L, Muzykantov V, Uvarov N and Argirusis C 2009 *Solid State Ionics* **180** 796

[29] Chefi S, Madami A, Boussetta H, Roux C and Hammou A 2008 *Journal of Power Sources* **177** 464

[30] Kendrick E, Sansom J E H, Tolchard J R, Islam M S and Slater P R 2007 *Faraday Discussions* **134** 181

[31] Yoshioka H, Nojiri Y and Tanase S 2008 *Solid State Ionics* **179** 2165

[32] Yoshioka H 2007 *J. Am. Ceram. Soc.* **90** 3099

[33] Kinoshita T, Iwata T, Bechade E, Masson O, Julien I, Champion E, Thomas H, Yoshida H, Ishizawa N and Fukuda K 2010 *Solid State Ionics* **181** 1024

[34] Sansom J E H, Kendrick E, Islam M S and Slater P R 2006 *J. Solid State Electrochem.* **10** 562

[35] Yoshioka H and Tanase S 2005 *Solid State Ionics* **176** 2395

[36] Ali R, Yashima M, Matsushita Y, Yoshioka H and Izumi F 2009 *J. Solid State Chem.* **182** 2846

[37] Nojiri Y, Tanase S, Iwasa M, Yoshioka H, Matsumura Y and Sakai T 2010 *J. Power Sources* **195** 4059

[38] Guo C J, Cai T X, Zhang W, Tian C G and Zeng Y W 2010 *Mater. Sci. Eng. B* **171** 50

[39] Kendrick E and Slater P R 2008 *Solid State Ionics* **179** 981

[40] Kendrick E and Slater P R 2008 *Mater. Res. Bull.* **43** 3627